Optical Microcavities for Enhanced Chemical Sensing

Naomi Omori

TRINITY COLLEGE

Supervisor: Jason Smith

Abstract

The following report showcases the successful proof of concept of a novel, tunable flow cell including an open access cavity array. A theoretical model to predict the relationship between the mode shift $\Delta\lambda$ and the change in refractive index Δn incorporating the effects of the penetration depth of the confined light into the distributed Bragg reflector within a Fabry-Perot microcavity is discussed. Designs of the flow cell with dedicated descriptions of each component are included. A shift related to a change in refractive index was observed by injecting saline solution into a cavity flooded with water. An agreement between the proposed theoretical model and the experimental data was observed for a penetration depth of L_{eff} = 0.33 μm. The results of this study characterize the novel device which will hopefully allow for the prediction of the detection limit of future prototypes.

Acknowledgments

Nine months ago I was swamped by an unerring sense of despair at the prospect of having to conduct my own research and produce a 12 000 word report discussing my findings. Luckily for me, most of my fears turned out to be unfounded thanks to the endlessly supportive network of colleagues and staff members I was lucky enough to work with throughout the year. Thanks first must go to my supervisor Dr Jason Smith for his patience, support, guidance and advice. Thanks also go to all members of the Photonic Nanomaterials Group for welcoming me into their lab, especially Johnny Fill, an endless source of entertainment, who on numerous occasions helped with my project when it wasn't his job to do so.

Particular thanks go to Dr. Phil Dolan who, having never met me, will never understand the extent to which I worshipped his PhD thesis and the amount of guidance it provided me with in my own project.

Pete Flaxman in the department workshop for his precision machining, Steve Lett for his good humour in allowing me to use the EM prep lab and Sverre Myrha whose supervision at Begbroke prevented me from damaging the AFM have all been indispensible and have earned my most genuine gratitude.

A heartfelt and most fervent thanks goes to Dr Aurélien Trichet, who has helped me and guided me from the beginning of this project in ways too numerous to express within the limitations of this word count.

Finally, and most importantly I thank my friends and family for their constant support regardless of the time or distance, for always being there to pick up the pieces and inspiring me to keep going. Eternal thanks go to my mother and my father Dr Masaharu Omori to whom this report is dedicated.

1   Introduction

This report delves into a small niche in the world of microcavity research. Extremely varied in their precise morphologies, microcavities are in essence mirror structures designed to capture and confine light. Prior to my arrival in the group, a new method of fabricating hemispherical optical microcavities into silica substrates had been developed. These microcavities are particularly interesting in that they are comprised of two independently tunable mirrors, which allow for an unprecedented level of control over the length of the cavity spacing with sub-micron level tuning precision. As this technology is relatively new, there is still huge scope within the group for a number of different projects where these microcavities form the heart, ranging from perfecting the fabrication technique to implanting the cavities with nanocrystals. An intrinsic feature of the open access nature of these particular cavities is that there is ample room for liquids to be freely flowed between the mirrors. Up till now, the preliminary characterization of these cavities in liquid had not yet been explored. My project was born out of the need to gain a greater understanding of the behaviour of these cavities in a liquid environment, with the aim of experimentally observing a change in the molecule concentration of a liquid that was been constantly flowed through the cavities. The project proved to be multifaceted, with elements of apparatus design, developing a new experimental method, theoretical derivation and lab-based experimentation.

1.1   Report Outline

In this report, I aim to assess the molecule detection capability of newly pioneered open access microcavities in aqueous environments. It was hoped that upon injecting fluids with a known impurity concentration into the cavities, the characteristic optical properties of the microcavities could be monitored to detect the amount of impurity present.

The report begins with a review of published literature. The first part looks at the use of Focussed Ion Beam (FIB) technology in the fabrication of different microcavities. The second focuses on where microcavity technology fits within the broader landscape of chemical sensing. It was necessary in both aspects of the literature review to include different types of

microcavities, as limited material exists for sensing using open access microcavities. Where possible, literature with at least one commonality with the setup employed in this project was selected.

Following this, a discussion of the theory governing the principles of the experiment is included. A theoretical model is proposed which explains the relationship between the observed resonant shift and the expected refractive index difference.

On the experimental setup front, I introduce the flow cell design used to conduct white light transmission experiments in a liquid environment, discussing briefly the challenges faced in bringing the design from paper to the lab. I present some preliminary refractive index sensing results using open access microcavities.

In the conclusion, I discuss some limitations of the current set up, and suggest possible paths for the next stages of experimentation.

1.2   Open Access Microcavities

Broadly speaking, an optical microcavity is a micron scale structure designed to capture photons within a confined volume for an extended duration of time. In the same way that the principals of quantum physics supersede classical physics as length scales are reduced, optical phenomena of interest begin to manifest themselves when cavities are fabricated on a micron length scale. Of particular interest is the length dependent resonant frequency spectrum that can be obtained when light is focused on a microcavity.

It is necessary to first briefly define some cavity metrics. A further discussion of these metrics can be found in 2.2. The quality of a cavity can be gauged by determining how long it is capable of confining light for. This can be described in terms of *cavity finesse* and the *Q factor*. In the field of microcavities, the quality factor, or Q factor, is the benchmark descriptor of the cavity in question, with literature commonly boasting about the use of 'high-Q microcavities'. Q factor describes the loss rate of light from a cavity. Values for Q factors

can vary widely from 10^3 to 10^8 for superior quality cavities. Finesse describes the loss rate of light as a function of the optical path length. Finesse values commonly range from 10^1 to 10^5. This project made use of a Fabry-Perot style microcavity, which is an arrangement of two parallel, independently tunable mirrors spaced microns apart, with a Q factor of around 10^5. For two planar mirrors, light confinement may be achieved in one direction perpendicular to the plane of the mirror. This premise is taken a step further by using instead of two planar mirrors in a parallel arrangement, a planar mirror on one side and a hemispherical mirror on the other. With this configuration, enhanced light confinement can be achieved in three directions.
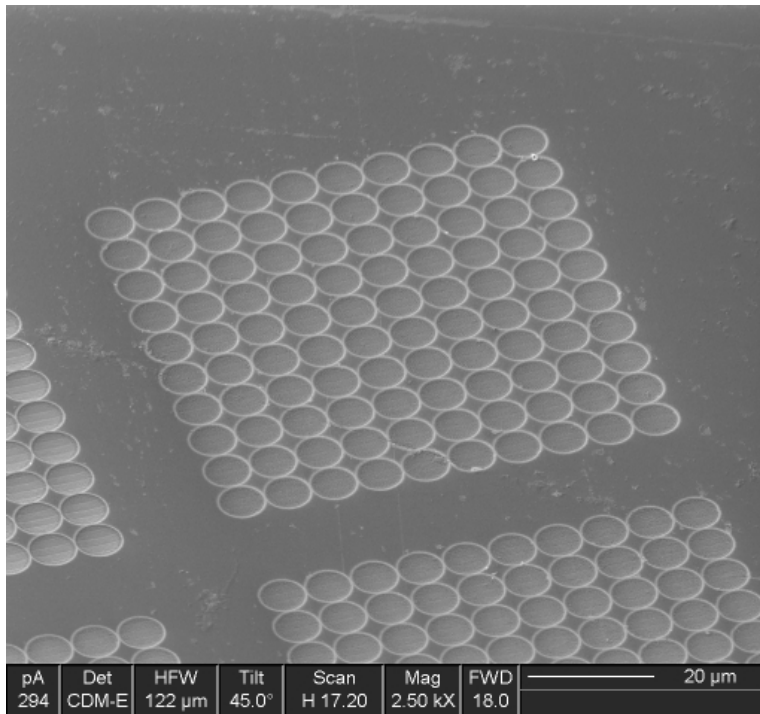

Figure 1: *SEM image of FIB milled hemispherical microcavities*

Figure 1 is a diagram of the open access microcavities used throughout this project. The hemispherical features can be seen in their arrays. In the following section, the fabrication method is explained.

1.3   Focused Ion Beam Fabrication

These fine hemispherical features are milled into fused silica substrates using a Focused Ion Beam (FIB) and then coated with a Bragg reflector to achieve the highly reflective surface required. With the Bragg reflector, hemispherical cavity arrays can be produced with reflectivity of up to 99.95%.

Some of the benefits of FIB milling include the extremely fine spatial resolution down to 10 nm, scalability and ease of use.

Similar to Scanning Electron Microscopy (SEM) where a beam of electrons rasters across the sample surface, the FIB scans a beam of focused gallium ions over the surface. Compared to SEM, the gallium ions being focused in FIB are of a much higher atomic mass than electrons. A sample is loaded into a vacuum chamber, which is held at a pressure of at least 2×10^{-5} Pa, and the beam is switched on. When the beam hits the sample, atoms are ejected from the surface into the surrounding vacuum. This process, called sputtering, occurs because the energy of the incoming atom has an energy comparable to the binding energy of the surface atoms. Like in SEM, backscattered electrons are also generated, and it is the signal from the electrons and sputtered ions that are used to image the sample. The sputtering means that unlike SEM, FIB is a destructive imaging method. The greater the degree of sputtering, the more the target substrate will be milled.

The degree of sputtering can be controlled by altering the beam current. If beam current is defined as [flux*beam area], by changing the aperture through which the beam is fed we have dynamic control over the beam current, ranging from 10 pA to 20 000 pA. As the beam current is increased, greater spread is seen in the spot size. As a general idea, imaging is usually carried out with a minimally destructive beam current of 30 pA. Targeted milling of features is carried out at higher beam currents in the range of 5000 to 20 000 pA.

The specific hemispherical features desired are milled into the target substrate by uploading a stream file into the FIB. Stream files contain information including a series of co-ordinates to define the beam path and a corresponding beam dwell time, which can be easily customized

to form different patterns. The cavities used for these experiments featured a diameter of 10 μm, radius of curvature of around 25 μm and depth of 500 nm and were milled in 3 x 3 arrays using a beam current of 20 000 pA.

The cavities used in this report do not represent the first attempt at fabricating microcavities using FIB technology. FIB milled cavities have appeared in a limited capacity in related literature since 2006 when Jiang *et al* used FIB to fabricate a photonic crystal microcavity array on a polystyrene film with a Q factor of 530 [2]. Cylindrical holes with 320 nm radii were milled. Their use of a significantly lower beam current of 30 pA is most certainly a function of the softer polymeric material they were milling into. Pillar microcavities were fabricated with FIB in 2007 by Kahl *et al* [3]. Ay *et al* also used a low beam current of 48 pA to mill Fabry-Perot waveguide grating structures into Al_2O_3 in 2009 [4]. However, published literature seems to indicate that the high-Q open access microcavities used in these experiments are the first to have been successfully fabricated using FIB. Indeed, this permutation of fabrication technique, cavity morphology and substrate material are completely unique in the current state of the art of microcavity technology.

1.4   Cavities in sensing

The amplified light-matter interaction capabilities of high Q microcavities combined with their low mode volumes and spectral selectivity make them promising for use in biosensing applications. Most optical biosensors aim to use a resonance shift from a change in refractive index as the main sensing mechanism. A wide range of cavity types are used including whispering gallery microspheres, microdisks, photonic crystals and microtoroids [11, 12]. A common concept in biosensing is 'label-free' vs. 'label-based' sensors. Label-based sensors involve attaching a marker, commonly fluorescent or enzymatic, to the target species. In this case, the target species is being indirectly sensed as the device is actually scanning for the label. Conversely, label-free sensors can directly detect the presence of the target species. The benefits of this include eliminating the process of finding appropriate markers tailored to the

target species and not having to alter the target species. While published literature has documented many successful attempts at label-free sensing, most of these have used approaches that could be defined as 'targeted' sensing [13]. The premise of most biosensing cavity papers hinges on having the target molecules adsorbing onto the surface of some part of the cavity. The thickening layer of adsorbed molecules serves to alter the local refractive index inducing a resonance shift within the system. In this respect, we can call this 'targeted' sensing, as although the analyte hasn't been treated with a marker, careful materials selection is required to find sensors that can preferentially sense specific molecules. Similar to label-based sensing, this mechanism is also fundamentally limited by the fact that specific analyte-sensor pairings need to be discovered for the sensing to work. As early as 2002 extremely sensitive protein detection using a resonance shift had been demonstrated by Vollmer *et al* [5]. A glass microsphere with whispering gallery modes was suspended at the centre of a flow cell through which an aqueous protein solution was passed. The protein would bind to the surface of the chemically modified silica glass surface causing a minute fluctuation in refractive index. It was shown that within this setup as little as 50 g/mol of bovine serum albumin (BSA) could be detected. In this configuration, analyte is being flowed around the outer surface of the cavity. Sensitivity in this set up is limited by the surface area available for molecule binding and the maximum density achievable taking into consideration factors such as crystallographically favourable bonding planes for the target species. A similar paper published in 2007 by Vincenti *et al* uses a surface interaction in a Fabry-Perot microcavity to present a modeling simulation of hydrogen detection for lactose malabsorption breath testing procedures [6]. Palladium plates, which absorb hydrogen spontaneously, are arranged parallel to one another. When H_2 gas impinges upon the Pd plate, palladium hydride (PdH) forms altering the dielectric permittivity compared to Pd, which in turn alters the refractive index by the relation $n = \sqrt{\varepsilon}$.

Guo et al established an alternative configuration for label-free Fabry-Perot biosensing in 2010 [7]. A method of fabricating a microcavity comprised of a large number of nanosized flow channels embedded within a borosilicate glass capillary with a highly reflective cladding

was presented, along with proof-of-concept results. A biolayer forms on the internal walls as protein loaded analyte is injected through the flow channels causing a shift in refractive index, which can be interpreted as a measurable resonance shift. This particular design has attempted to maximize the surface area for protein binding available to the analyte in an extension of the concept explored earlier by Vollmer *et al* [5]. This method is shown to have a sensitivity of 550 nm/RIU. Beyond demonstrating a device with impressive sensitivity that yields results within minutes of initiating analyte flow, Guo *et al* have developed a glass drawing fabrication technique that is rapid, cost-effective and scalable with production viability beyond the laboratory. The design is arguably limited by the fact that although cavities of different specifications could theoretically be fabricated quite easily, the cavity length is ultimately not tunable once the capillaries have been drawn.

Dorfner *et al* more recently in 2011 used a photonic crystal cavity array to test for BSA in aqueous solution [8]. Similar to Guo *et al*, this publication was experimenting with another type of integrated liquid flow cell. Rather than direct individual channels through the cavities, Dorfner *et al* used a similar approach to that used in this project where an open access flow cell over a photonic crystal was developed in the hopes that the technology could be more seamlessly incorporated into lab-on-chip applications in the future. Electron beam lithography and reactive ion etching was used to fabricate the hexagonal pattern of cavities. Their preliminary refractive index sensing results, where water was injected into an empty photonic crystal and a resonant shift was recorded, were carried out in a very similar manner to how refractive index was measured in this project. For a shift from air to water, a resonant shift of 33 nm was recorded. Their results showed that this type of cavity has a sensitivity of 103 nm/RIU. Tomljenovic-Hanic *et al* also flushed an ultra high-Q photonic crystal cavity with water to observe a resonant shift in 2013 [9]. Their microcavities featured an impressive Q-factor of 10^6. This paper also featured a shift from air to water, as is common in a few papers (refdorf). This is likely because $\Delta n = 0.333$ is very large so an easily resolvable resonant shift should be observed.

A conclusion of the state of the art in microcavity sensing might be that the field is quite varied. Literature has documented the use of a wide variety of cavities, with a varied spectrum of sensitivities. As a dynamic field that has seen a peak in interest over the last decade, there is just enough knowledge available for current groups to steer further research towards real world applications. This is certainly the case in biosensing, which takes the basic physics-based principles of cavitation and paves the way towards more interdisciplinary technologies that begin to incorporate elements of biology and chemistry. At the same time, the field is not burdened by the gravity of decades of established research, so even some of the most recent papers are only providing preliminary proof-of-concept results for new ways of approaching the construction and use of microcavities [9]. In biosensing, almost all papers have used the principles of ligand adsorption to observe a resonance shift. It is almost certain that no published literature has included experimental results from the combination of features present in this set up. Unique to this project is the use of open access cavities with a flow cell. While open access flow cells that feed fluids through the microcavity have been tested previously, the mirrors used in this project have a huge degree of online tunability. Resonance shifts from refractive index results are included in this project, however the shift observed is not as a result of layers being deposited on the surface of the mirror, but rather by a total change in the effective refractive index of the volume of the liquid.

1.5   Engineering Relevance

On a broader scale, there has been a recent movement towards research into portable, personalized medical diagnostic tools with a user-friendly interface. Only very recently in January 2012, the Qualcomm Tricorder X Prize was announced where a prize would be awarded to the team that could design a tool capable of diagnosing a set of common diseases as well as measure fundamental health metrics such as respiratory rate [16]. In the statement released explaining the genesis of such a competition, the need to 'tackle breakthroughs in sensing technologies [and] technological integration' as well as 'making health a willing part of individuals' daily lives' were cited as reasons, highlighting the current healthcare system's

desire for integrated sensing devices. Even within the scientific community, journal articles expressing the need for "personalized medicine" devices using label-free microcavity biosensors have been published. In 2012 Amarie *et al* argue in depth the benefits of exploring microcavity technology capable of sensing down to single molecules to understand the mechanisms of disease proliferation, with a view to incorporate into personalized diagnostic devices that would allow patients to monitor their own health outside of the doctor's office [10].

Although the experimental results obtained in this project only serve as proof of concept, microcavities possess some unique and exciting features that could potentially see the technology being incorporated into highly marketable sensing devices for use in applications such as medical diagnostics, water testing and breath testing. In particular however, this technology has not been characterised as a biosensor, although theoretically functionalizing one or more of the reflective surfaces could transform the cavities transformed into targeted biosensors, working on principles similar to those discussed in chapter 1.4.

Open access cavities integrate well with microfluidic systems, as they have a comparably large flow through area, which can be easily coupled into channels. This is important for medical diagnostics where sensing of water based samples is required.

Cavities have low mode volumes in the order of femtolitres meaning only a small sample volume is required for testing. This would be ideal, for example, in the field of hematology where occasionally obtaining large specimen volumes may be problematic, which is often the case with pediatric or geriatric phlebotomy collections.

The high degree of online tunability also makes this technology capable of sensing a wide range of molecules as there is a large degree of control over the cavity length.

From a production standpoint, despite being such a delicate structure this fabrication method for this type of microcavity is fast and scalable. It also doesn't require specific expertise from a technician to fabricate, as once stream files have been optimized, the FIB computer system can automatically mill many hundreds of the hemispherical arrays by itself. This is attractive for future applications where mass production becomes a concern.

2   Theoretical Principles of Cavity Sensing

2.1   Theoretical Relation Between a Resonance Shift, Refractive Index and Penetration Depth

Fundamental to any discussion concerning microcavity experimentation is the characteristic frequency spectrum obtained and the concept of cavity modes.

A cavity mode is the standing wave formed by light confined between the mirrors of the cavity as a result of destructive and constructive interference. Consider a simple cavity of two parallel, planar mirrors with a separation distance, or cavity length of L, bounding a light-propagating medium of refractive index n. Light enters the cavity perpendicular to the plane of the mirror and is bounced back and forth between the two mirrors. A standing wave will form as a result of interference between two identical waves moving in opposite directions. The distance between two nodes in a standing wave is always $\lambda/2$. It follows then that for standing waves to fit within the cavity, that is for specific cavity modes to exist, the cavity length L must be equal to an integer multiple of half the wavelength of light λ.

$$L = q\frac{\lambda_m}{2} \tag{2.1}$$

In other words, cavity wavelengths are dependent on the length of the cavity. The integer multiple q is called the mode number and can be thought of as the number of half wavelengths present in the cavity. Rearranging we can form an expression for the wavelength of the mode.

$$\lambda_m = \frac{2L}{q} \tag{2.2}$$

It should be noted that λ_m refers to the wavelength travelling through the medium present within the mirrors. This is because a modification for the refractive index needs to be taken

into account when light is propagating through a medium. Equation 2.2 can be re written in terms of the wavelength of light in a vacuum, λ_0.

$$\lambda_m = \frac{\lambda_0}{n} \qquad (2.3)$$

$$\lambda_0 = \frac{2nL}{q} \qquad (2.4)$$

This is the basic expression for the wavelength of a longitudinal cavity mode. Longitudinal modes are waves confined along the length of the cavity, perpendicular to the plane of the mirror. It is possible to also see transverse mode excitation, that is modes appearing perpendicular to the direction of the longitudinal modes. Note that this model so far is for two planar parallel mirrors, which doesn't feature transverse mode excitation. In a hemispherical mirror configuration however, we will. A more complete expression of the wavelength of a cavity mode would incorporate both the longitudinal and transverse components:

$$\lambda_0 = \frac{2nL}{q + \frac{1}{\pi}(m + n + 1)\cos^{-1}\sqrt{g_{Pl}g_{Hem}}} \qquad (2.5)$$

where q is the longitudinal wave number and m & n are the transverse mode numbers. This expression introduces parameters that deviate from the model expressed at the beginning of the chapter. In the beginning we assumed the simplest case of two parallel planar mirrors. In reality, the cavities in question are comprised of one planar mirror and one hemispherical mirror. g_i refer to the resonator parameters and can be defined as $g_i = 1 - \dfrac{L}{R_i}$, with R_i representing the radius of curvature of the mirror. In the case of the planar mirror $g_{Pl} = 1$, as the radius of curvature is 0. The transverse component tends to be omitted in the analysis of data in this project as longitudinal modes can be readily imaged and appear as the stronger mode in white light transmission spectra. As a result, in experimentation it is the longitudinal modes that are selected, as they are the easiest to monitor. As such the transverse component has been omitted in these equations.

Equation 2.4 can be further manipulated to express the more direct relationship between refractive index and wavelength, which formed the basis of this project. For a selected cavity mode, L and q can be considered as constant values. Differentiating we obtain:

$$\Delta\lambda_0 = \frac{2\Delta n L}{q} \qquad (2.6)$$

$$\frac{\Delta\lambda_0}{\lambda} = \frac{\Delta n}{n} \qquad (2.7)$$

Equation 2.6 shows that we should expect to see a direct linear proportionality between a change in refractive index and a change in the resonant wavelength of a cavity mode. In equation 2.7 the constant term $\frac{2L}{q}$ is eliminated to produce the relationship between wavelength and refractive index. In theory, we should be able to predict an experimental resonance shift given that difference in n between the fluids to be injected inside the cavity is a known value.

It transpires, however, that this relation is not completely sufficient to make accurate predictions for wavelength shift. This is because the penetration depth of light into the distributed Bragg reflector (DBR) coating has not yet been taken into account. Penetration depth is a measure of the distance beneath the surface at which the evanescent light beam dissipates to 1/e of its original intensity at the surface.
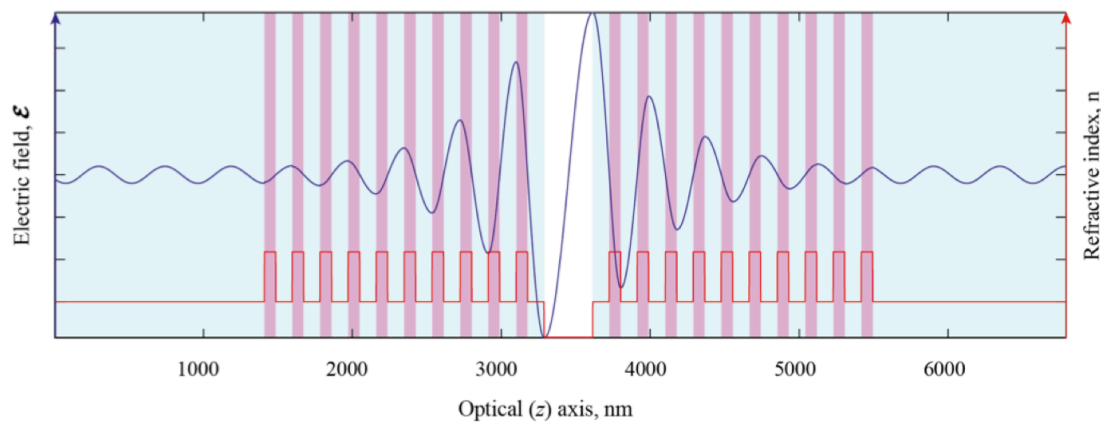

Figure 2: *Penetration depth of light wave into a distributed Bragg reflector. Reproduced from [1]*

This means that as the cavity spacing becomes shorter, standing waves are no longer totally bounded by the mirrors as an exponentially decaying component of the waves extends into the DBR. As a result, the cavity length as defined simply by the distance between the mirrors becomes less relevant. An effective cavity length L_{eff}, which describes the penetration depth needs to be considered.

A short aside on the structure of a DBRs; distributed Bragg reflectors are highly reflective mirror structures comprised of multiple alternating layers of two different optical materials. Between the two optical materials, there is a significant difference in refractive index such that one material has the higher refractive index, n_H, and the other is identified as the lower refractive index material, n_L. DBRs work on the principle of constructive interference. A schematic of a DBR is illustrated below. The alternating layers are depicted to have a periodicity of Λ, with s marking a step from a low refractive index medium to a high refractive index medium.
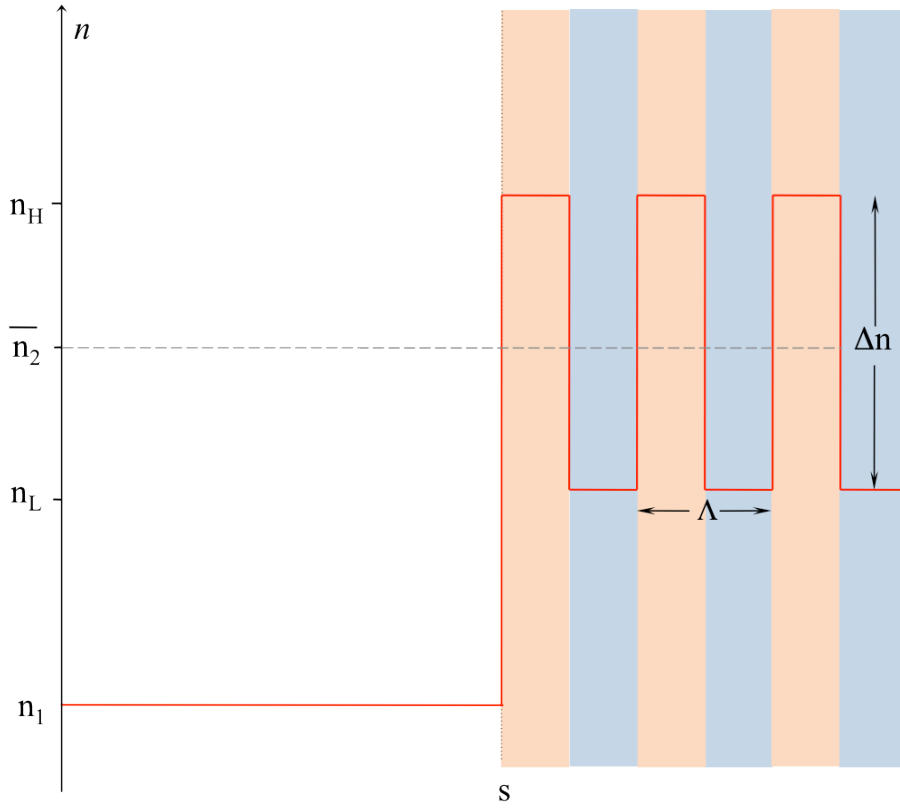
Figure 3: *Schematic of a DBR defining refractive index terms used in equation 2.8 & 2.9*

An expression for the penetration depth of a Bragg mirror by Brovelli *et al* is used in the calculations of the penetration depth [14]. L_{eff}, which describes the penetration depth into the DBR, can be expressed as follows:

$$L_{eff} = \frac{n_1 \lambda_B}{4 \bar{n}_2 \Delta n} \qquad \text{for s = 0} \qquad (2.8)$$

$$L_{eff} = \frac{\bar{n}_2 \lambda_B}{4 n_1 \Delta n_B} + \frac{\lambda_B \Delta n_B}{2\pi^2 n_1 \bar{n}_2} \qquad \text{for s = Λ/2} \qquad (2.9)$$

where n_1 is the refractive index of the substrate the DBR is deposited onto within the cavity, and λ_B is the central wavelength of the photonic stopband of the DBR. The separate equations refer to the periodicity of the stack. Equation 2.8 can be applied when the layer bounding the substrate is of the higher refractive index. Equation 2.9 is applicable when the layer next to the substrate is of a lower refractive index. The reflectors used in this project were designed such that an anti-node was sitting on the surface of the reflector, meaning the

topmost layer of the DBR is the lower refractive index material n_L. Therefore equation 2.9 is most relevant for this project. It is not sufficient to stop at an expression for L_{eff}, however, as penetration depth and the refractive index of the material into which the wave encroaches are intrinsically intertwined quantities. A more all-encompassing approach would be to consider cavity separation and refractive index as the single entity of the optical path length. This reconceptualisation is necessary to incorporate the penetration depth into the path traversed by the light. So far the optical path, l, is defined as:

$$l = nL_0 \tag{2.10}$$

where L_0 is purely the length of the spacing between the two mirrors. With penetration depth included, the characteristic optical path of light within a Fabry-Perot microcavity, which we will now refer to as L_{opt}, can be defined as:

$$L_{opt} = nL_0 + 2\bar{n}_2 L_{eff} \tag{2.11}$$

A factor of two is added to include the penetration depth into both the top and bottom mirror. Now, any undefined L from equations 2.1 up to 2.9 can be replaced with L_{opt}. Using equation 2.2 and rearranging in exactly the same way as equation 2.7 was achieved by eliminating the term $\dfrac{q}{2}$, a relationship between L_{opt} and λ can be defined.

$$\frac{\Delta\lambda}{\lambda} = \frac{\Delta L_{opt}}{L_{opt}} \tag{2.12}$$

Derive 2.11:

$$\Delta L_{opt} = L_0\Delta n + n\Delta L_0 + 2\bar{n}_2\Delta L_{eff} \tag{2.13}$$

$$\Delta L_{opt} = L_0\Delta n \tag{2.14}$$

We may reduce ΔL_{opt} to its form in 2.14 as L_0 and L_{eff} are both constant terms, hence their derivatives cancel to zero. Substituting 2.14 back into 2.12 we obtain:

$$\frac{\Delta\lambda}{\lambda} = \frac{L_0\Delta n}{L_{opt}} \tag{2.15}$$

Further to this, we can normalize this relation in 2.15.

$$\frac{\Delta\lambda}{\lambda} = \frac{\Delta n}{n}\left(\frac{nL_0}{L_{opt}}\right) \qquad (2.16)$$

We are left with a relation reminiscent of that in equation 2.7, but with an additional scaling factor highlighted within the parentheses, forthwith called the compensation factor f_c. With equation 2.16, we return to the original statement made after the presentation of equation 2.7 that the penetration depth of the DBR needs to be considered for an accurate relation between a resonant shift and a shift in refractive index. A rearrangement of f_c is made using equation 2.11 to elucidate the relevance of L_{eff}, and to have an expression that dovetails neatly with any experimental data obtained, as L_0 is not a directly measurable quantity.

$$f_c = \frac{L_{opt} - 2\bar{n}_2 L_{eff}}{L_{opt}} \qquad (2.17)$$

The nature of the compensation factor may be expressed in the following limit:

$$\lim_{L_{eff} \to 0} f_c = 1 \qquad (2.18)$$

As the penetration depth decreases and tends towards 0, the compensation factor tends towards 1. In this instance, equation 2.16 becomes consistent with equation 2.7.
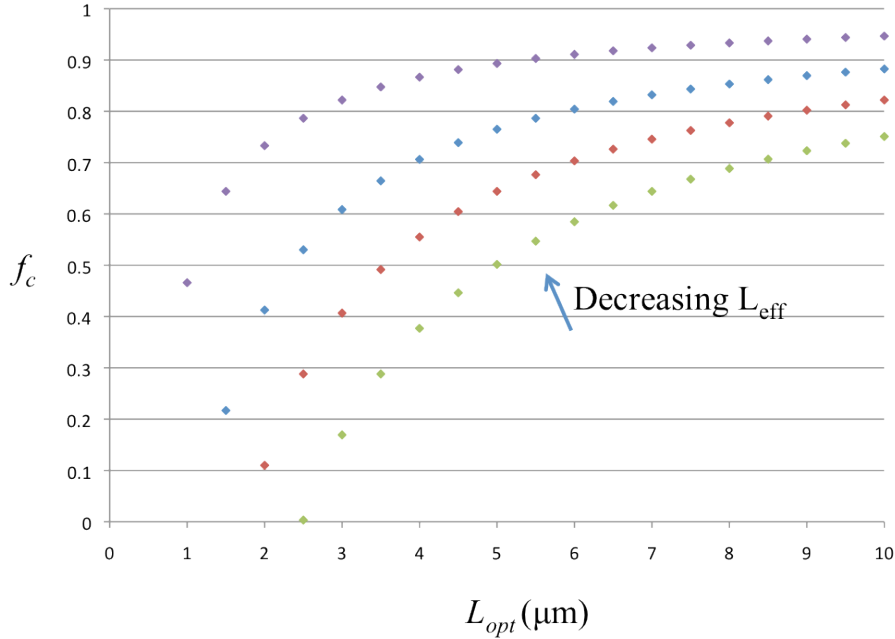

Figure 4: *Plot of compensation factor against optical length for a series of different penetration depths*

A plot of the compensation factor against optical length using the penetration depth given in equation 2.9 for a series of arbitrary penetration depths shows that for longer cavity lengths, the effect of the compensation factor becomes less. The green plot represents the largest penetration depth, with the purple plot representing the lowest penetration depth. This compensation factor does not depend on refractive. It is a universal curve that works for any material inserted into the sensor.

2.2   Cavity Metrics

An extended discussion on the cavity metrics briefly described in section 1 are included in this section. A white light transmission spectra is introduced. This is the raw experimental data from which we are able to assign physical meaning to the theoretical metrics discussed below. Wavelength increases from left to right and light intensity increases from bottom to top.
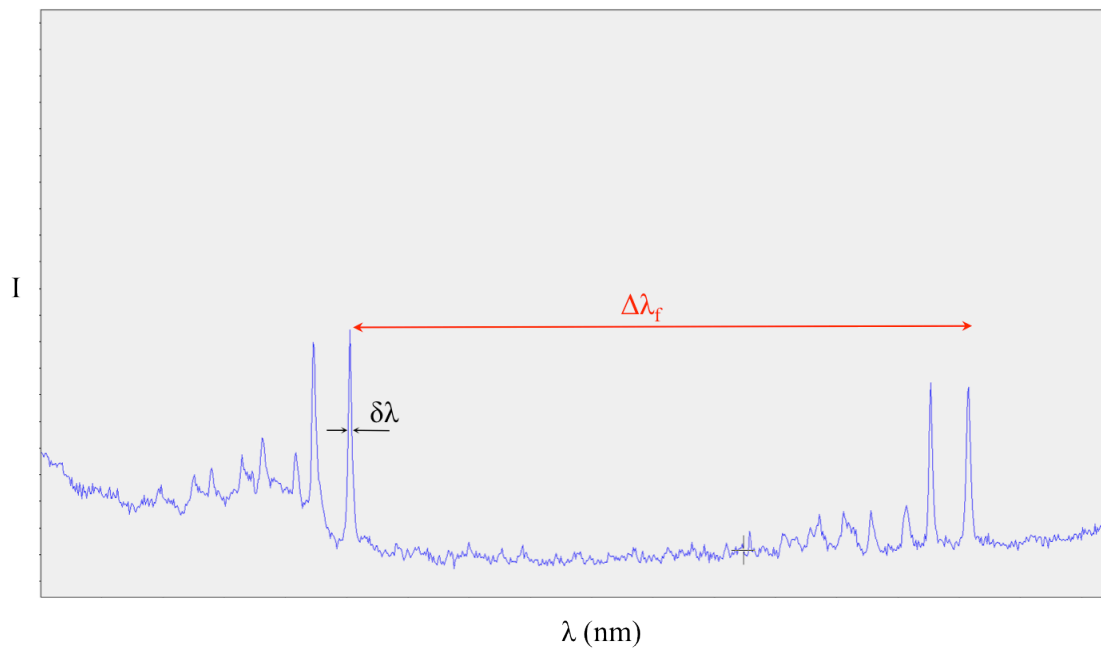

Figure 5: *White light transmission spectra including longitudinal and transverse modes*

The peaks observed are the resonant cavity modes discussed in 2.1. We are concerned with the longitudinal modes, which are the tallest, most intense modes. A 'resonant shift' refers to an observed shift to either the right or left depending on whether the wavelength of these peaks is increasing or decreasing. In this experimentation, we ultimately resolved a shift to

21

the right as the cavity modes moved to a higher wavelength upon the introduction of a high index refractive medium into the cavity.

The free spectral range (FSR) $\Delta\lambda_f$ is the spacing between two optical intensity maxima. Specific to the resonant frequency spectrum of microcavities, $\Delta\lambda_f$ can be obtained by measuring the spacing between two consecutive modes. The FSR is used to obtain the optical path length of the cavity, L_{opt} with the relation:

$$L = \frac{\lambda^2}{2\Delta\lambda_f} \tag{1.1}$$

$\Delta\lambda_f$ is not to be confused with the resonant shift $\Delta\lambda$. FSR refers to a spacing between two separate peaks. $\Delta\lambda$ on the other hand measures the shift experienced by a single peak over time.

The other term pictorially defined on the transmission spectra above is $\delta\lambda$ or the full width at half maximum (FWHM).

Consider that a perfect microcavity would be able to contain light for indefinite amounts of time. In reality light will always be lost, but at different rates depending on the quality of the factor, with more perfect cavities confining light for longer. The Q factor, therefore, quantifies as a function of time, the loss of light from a cavity. In physical terms, it describes the number of round trips a photon will make around the cavity before leaking out. In more mathematical terms this could be expressed as:

$$Q = \frac{U(t)}{-\left(\frac{dU(t)}{dt}\right)}\omega_0 \tag{1.2}$$

where $U(t)$ is the total energy of the light and $-(dU(t)/dt)$ describes the energy lost with each oscillation frequency ω_0. Q factor may also be defined further in terms of energy storage:

$$Q = 2\pi \frac{energy\ stored\ in\ cavity}{energy\ lost\ per\ photon\ cycle} \tag{1.3}$$

$$Q = 2\pi \frac{cE}{\lambda_0 P} \tag{1.4}$$

where P is the power dissipated and E is the energy stored in the cavity. It can also be defined with respect to the resonance bandwith:

$$Q = \frac{\lambda}{\delta\lambda} \qquad (1.5)$$

This defines the Q factor as the peak resonance as divided by the FWHM. In defining the Q factor, it is most important to recognize that this metric specifically describes the rate at which light is being lost from the cavity. It is easiest to appreciate this from the differential equation 1.2.

Finesse measures the rate at which light escapes from a cavity per round trip of the photon. It can be described as the free spectral range divided by the FWHM:

$$F = \frac{\Delta\lambda}{\delta\lambda} \qquad (1.6)$$

Free spectral range is a length dependent quantity, so in analyzing finesse, we may have infer a more detailed picture of the mechanisms of loss rate. Q factor, while similar in the sense that it describes a loss rate, is not length dependent, meaning that increasing the Q factor by changing the length is not immediately evident.

3 Experimental Setup

3.1 Flow Cell

A disassemblable flow cell was designed in order to pass liquids through an open access microcavity system. The goal of the flow cell was to create a leak-proof, liquid environment surrounding the Fabry-Perot set up. The challenge in designing the cell was to maintain the high degree of cavity length tunability specific to open access microcavity technology. In standard microcavity analysis, tunability in three dimensions was achieved by mounting the featured and planar mirror directly onto an actuator and z-positioner respectively. In the final design of this project, the mirrors were mounted instead onto two plates separated by a rubber seal, forming a flow cell. This cell was mounted between similar x-y-z postioners, providing the full range of tunability.
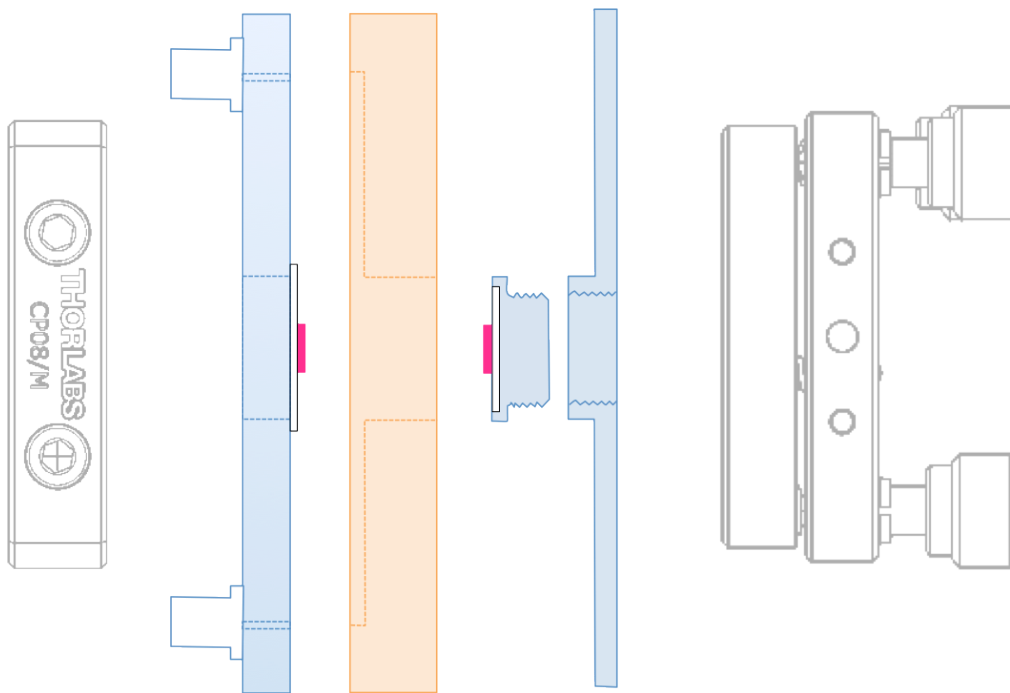

Figure 6: *Exploded view of setup including cage plates, actuator and flow cell components. Cage rods have been omitted for clarity. The pink rectangles represent the mirrors.*

24

3.1.1 Top Plate

The top plate was a 4 mm thick clear polycarbonate strip into which inlet & outlet holes were drilled, along with an aperture for the light path. The aperture was necessary, as despite it being transparent, the refractive index of the polycarbonate would have interfered with results. On the exterior face, two nanoports were glued on with cyanoacrylate. The nanoport assembly consisted of an internally threaded port and matching ferrules, which could be affixed to the ends of tubes. It served as an easy method of coupling tubing in and out of the cell in a liquid fast fashion. On the opposing side a cover slip with the featured mirror was mounted over the aperture. The cover slip was permanently bonded to the polycarbonate with cyanoacrylate. It was necessary for a non-permanent bond between the featured mirror and the glass cover slip. This was because the process of achieving the micron spacing between the mirrors sometimes resulted in mirrors breaking if the surfaces ended up touching. For this reason silver dag was used.
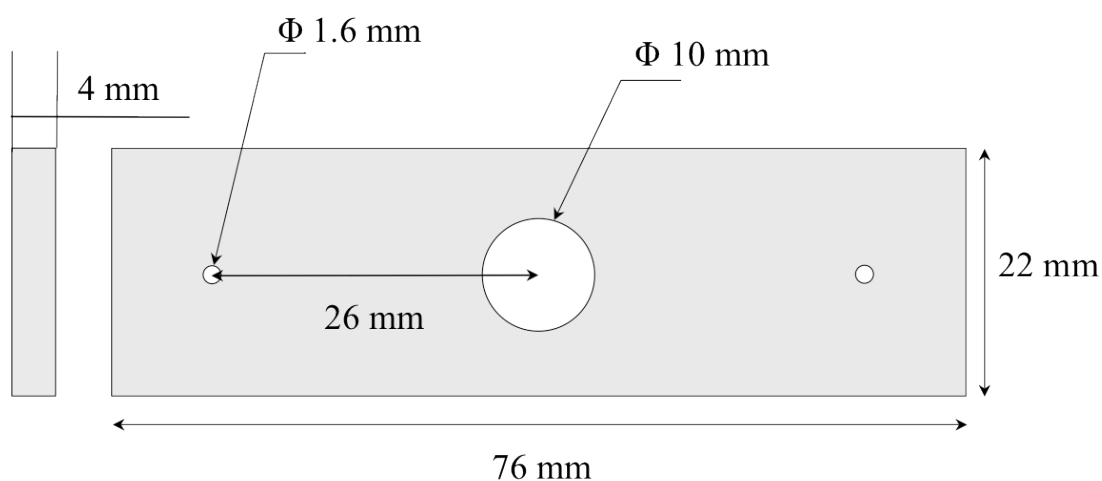

Figure 7: *Dimensions of top plate*

3.1.2 Fluid Tight Seal

Silicone rubber was selected to provide the fluid tight seal, on the basis that upon compressing the device, the material would expand laterally filling up any gaps where liquid might escape. 6 mm silicone rubber sheeting was purchased from a manufacturer. The characteristic shape of the seal allowed for coarse positioning of

the flow cell and cavity stabilization in the x-y direction as the winged edges nestled between the cage rods limited the range for drift. A 19mm circular stamp was commissioned from the workshop to cut an aperture that fit snugly around the plinth. The channels were cut in by hand with a scalpel to half the depth of the rubber. The particular dimensions of the perimeter were channels were arbitrary. A channel length of 21 mm was selected to ensure the ports from the top plate could feed into them.
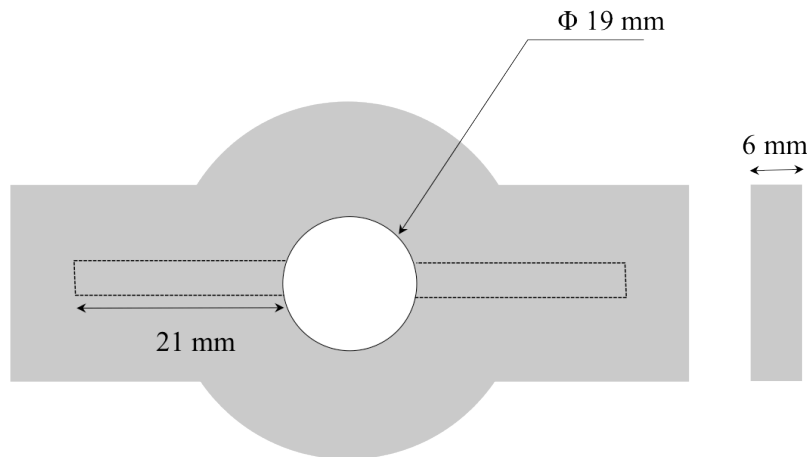

Figure 8: *Dimensions of rubber seal*

3.1.3 Bottom Plate

The bottom plate featured an adjustable plinth upon which the planar mirror was mounted. The plinth design arose from the need to at once achieve a microscopic spacing between the mirrors, but also a macroscopic scale thickness over which compressive forces could be applied to seal the silicone rubber. It was comprised of a bottom plate with plinth standing proud around the aperture and an internal thread. A separate cap was designed to be screwed into the plinth, such that the total height of the column was adjustable to accommodate substrates of different thicknesses. The cap of the plinth was machined with an aperture over which a cover slip was mounted, similar to the top plate. Polytetrafluoroethylene (PTFE) thread seal tape was used to eliminate leaks through the plinth. With this design, the plinth has a height range of 3.6 – 5.6 mm.
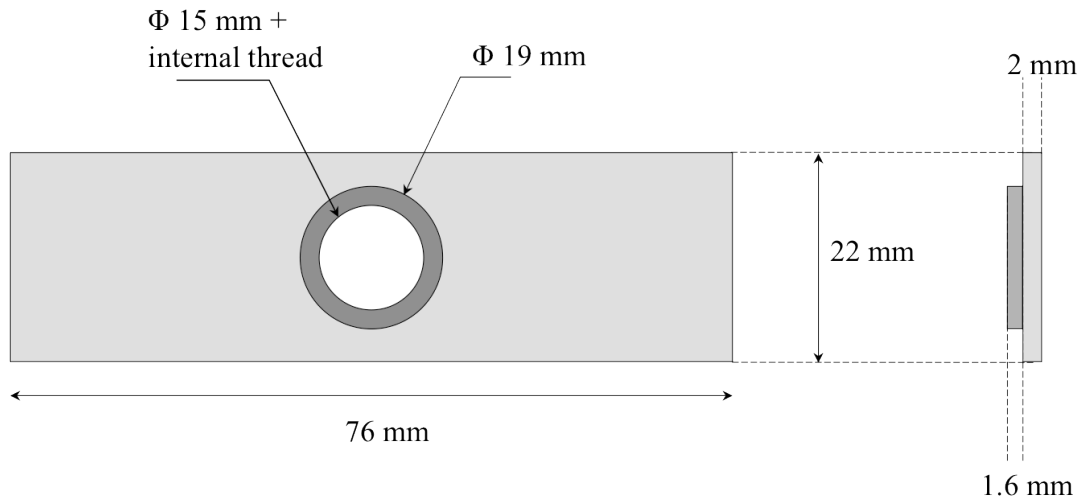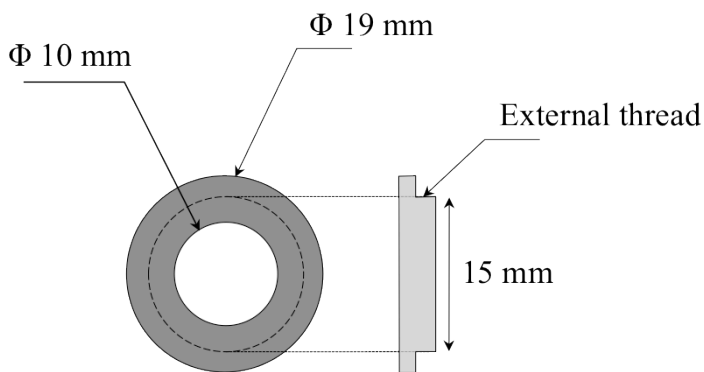
Figure 9: *Dimensions of bottom plate*

Figure 10: *Dimensions of cap to be screwed into the bottom plate to form the height adjustable plinth onto which the planar mirror was mounted*

The flow cell was assembled by pushing the rubber seal over the plinth and aligning the aperture on the top plate with the aperture on the bottom. This device was then mounted vertically between cage rods with the top plate against a fixed cage plate and the bottom plate braced against a kinematic actuator. The featured mirror was adhered to the top plate due to the working distance of the objective lens. The height of the plinth proved prohibitive when attempting to focus the cavities with the objective lens.

Figure 11: *Photograph of flow cell. The diminutive size of the featured substrate visible in the middle of the top plate can be appreciated. The rubber seal has been fitted over the plinth*

Tuning cavity length

Exploiting the kinematic actuator design served multiple purposes, providing both the coarse and fine tuning of the cavity lengths as well as generating the compressive force required to squash the silicone rubber seal. For coarse tuning, the screws of the actuator were wound back as far as possible and the stage then pushed as close as possible to the flow cell along the cage rods by hand. By turning each of the three screws by equal amounts the stage could be moved uniformly against the cell causing the device to compress. This process was continued until etalon fringing became visible on the webcam. From this point, fine-tuning was carried out iteratively by tweaking screws individually and observing the shift in fringes until the desired spacing and tilt was achieved. Micron scale precision could be achieved between the cavities using only this actuator.
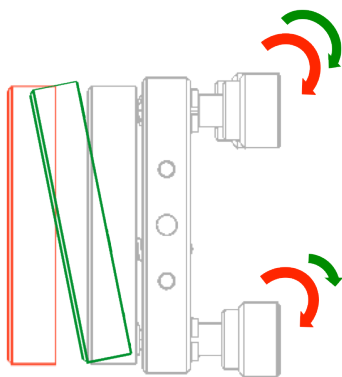

Figure 12: *Visual aid to describe how one kinematic actuator can be used to both tilt and compress the sample*

28

3.1.4   Fluidic System

The set up developed provided a reliable way of achieving stable modes. Injecting fluid into the cavity with a syringe by hand highlighted the need to establish a constant flow so as not to upset the modes being imaged. The cavity setup proved highly sensitive to fluctuations in pressure as extreme shifting of modes was observed, likely as a result of cavity length changing as the water pressure pushed the substrates apart. The aim therefore was to be able to flood the whole cavity at a constant pressure where cavity length could stabilize for the duration of the experiment.

Low volume green microfluidic tubing with an inner diameter (ID) of 0.16 mm was coupled directly into the cell. The rubber tubing coupling the green tubing into the syringe also acted as a dead volume promoting a steady flow into the narrow microfluidic tubing. An automated syringe pump from KD Scientific provided a steady flow rate of 0.2 mL/min. Liquid was fed into the cell from the bottom up, ensuring that the backpressure distributed liquid through the cavities evenly. If injected from the top, liquid would take the path of lowest resistance around the perimeter of the plinth, failing to flood the space between the mirrors. Waste was siphoned off into a beaker.

3.1.5   Materials Selection

The choice of materials for this cell was dictated by design and manufacturing limitations. Polycarbonate was initially chosen for its transparency and toughness. A transparent top plate was desired so liquid flow through the cell could be monitored. Toughness was also important as the device was going to be subjected to considerable compressive forces. Polycarbonate is also inert. The selection of acrylic for the cap on the plinth was upon the request of the workshop as machinable polymers were preferred for the manufacture of such small-scale components.

If a second version of this flow cell were to be produced, it might be preferable to select a polymer that is more resistant to solvent attack, as currently the device is only appropriate for

sensing of chemicals in aqueous solution. Polyether ether ketone (PEEK), which is what the tubing and nanoports were made of, might be an option.
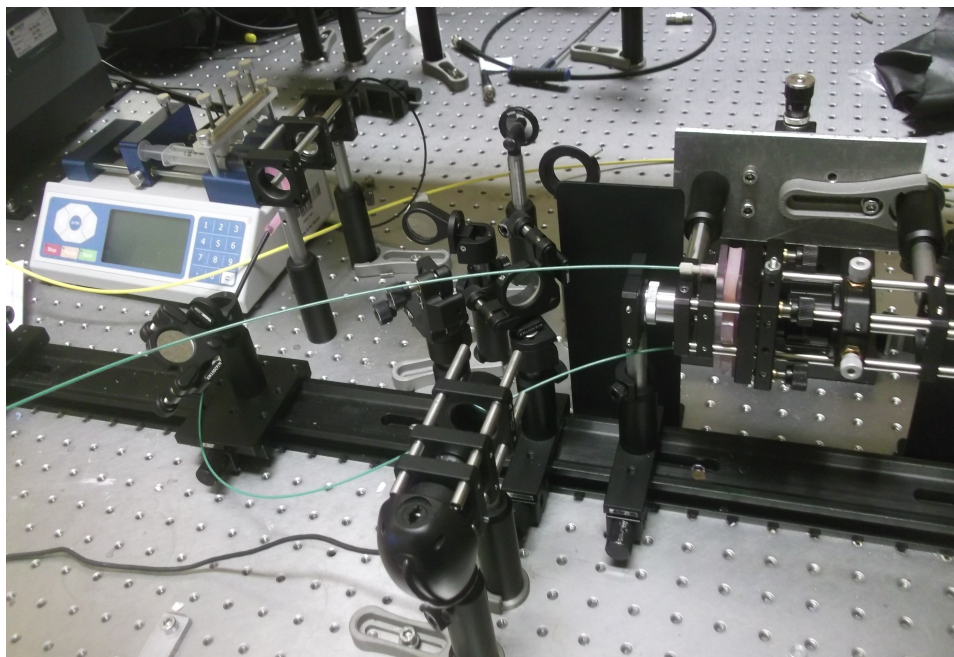

Figure 13: *Photograph of the experimental setup. In the upper left corner the syringe pump is visible with green tubing already connected. On the right hand side the flow cell can be seen vertically mounted into the cage rod system.*

3.2 White Light Transmission Set Up

A series of lenses was used to focus a free space coupled Bentham WLS100 white light source onto the cavities. A Thorlabs optomechanic cage rod & optical rail system provided the skeleton onto which lenses and positioning components were mounted.
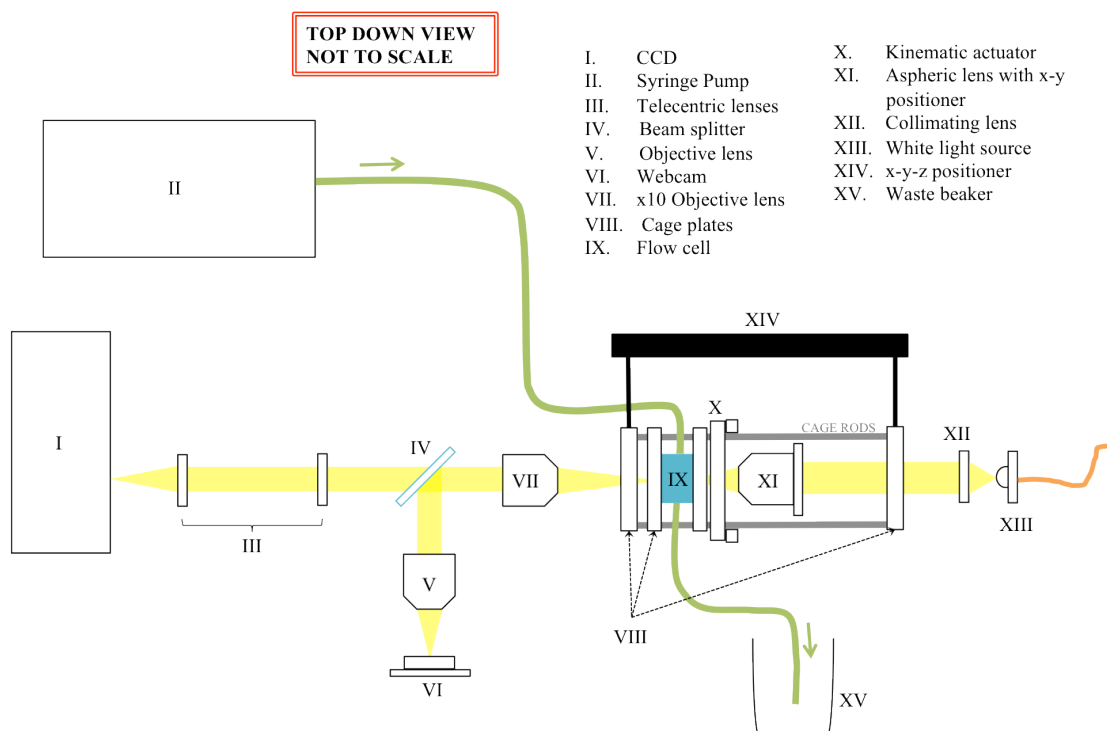
Figure 14: *Schematic of the experimental set up showing the light path through the lens set up*

The fibre optic plugged into the white light source was mounted on an optical post onto the rails. To maximize the light hitting the sample, a free standing collimating lens was aligned adjacent to the white light source. The collimated light was fed into a cage-rod mounted aspheric condenser lens. The aspheric lens was attached directly to an x-y translator, which directed the focused beam to the desired position on the substrate. As discussed previously, the flow cell was mounted onto these cage rods between a cage plate and kinematic actuator. The whole cage rod configuration was mounted onto a larger x-y-z translation stage, which allowed for the focusing and positioning of the cavities relative to the freestanding objective lens. A glass beam splitter enabled simultaneous imaging of the cavities onto a webcam and onto the CCD.

4 Results

4.1 Introduction

The results of the following room temperature experiments were obtained by injecting saline solutions into a flow cell full of distilled water. If the refractive index of the medium between the mirrors is increased from $n_{H20} = 1.3330$ to a higher refractive index saline solution, the imaged modes of the resonant spectrum should shift to a higher wavelength.

Two experiments were executed; one where L was kept constant, and a second where L was varied.

As established earlier in the theoretical discussion, the resonant spectrum of a microcavity is dependent on a series of refractive indices n_i and the optical path length L_{opt}. At this point, it may be useful to summarise the main parameters of this setup.

A stack of silica ($n_L = 1.46$) and zirconia ($n_H = 2.1$) was used to produce a reflectivity of 99.95% and a peak resonance at around 640 nm. Three concentrations of saline solution were used. 26 g/100 mL represented the saturation limit of salt in distilled water at room temperature.

Table 1: *Refractive index table of liquids tested. Reproduced from [17]*

Salt Concentration (g/100mL)	n_1
20	1.3684
15	1.3594
13	1.3558
Distilled Water	1.3330

4.2 Length Independent Time Delay of Resonant Shift

To ensure the resonant shift observed was a function of saline solution entering the cavities, the cavity arrays were oriented such that a time delay could be observed. The apparatus was aligned such that multiple cavities were sitting parallel to the CCD slits, stacked perpendicular to the fluid front. The mirrors were made as parallel as possible, so that there was no variation in L across the multiple cavities being imaged. It was postulated that using this set up, due to the staggered position of the cavities relative to the incoming saline front, a

time delay spread in the shift of the modes would be observed. If L is constant, we could expect to see a similar resonance.
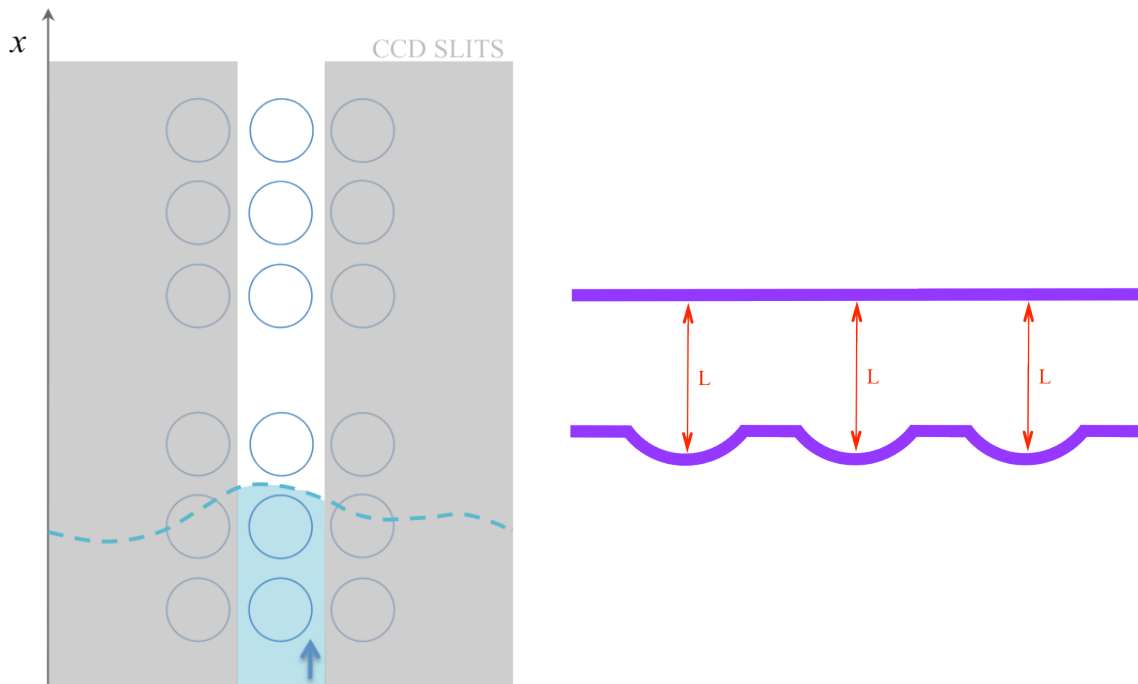

Figure 15: *Diagram showing a) orientation of cavities relative to CCD slit and direction of liquid flow and b) parallel configuration of mirrors of the microcavity for this data set*

Six modes were tracked with cavity lengths calculated from the free spectral range, as summarized in table 1.

Table 2: *Cavity lengths highlighting the parallel nature of the mirrors in this experiment*

Track	Length (μm)
1	2.286
2	2.314
3	2.300
4	2.281
5	2.267
6	2.256

A spread in the range of cavity lengths of only 58.13 nm exists, which is minimal. A colourscale plot of the modes in track 5 is pictured below. In the spectral videos taken, a series of 4000 transmission spectra of λ vs light intensity as depicted in figure 1, integrated over a selected time of 0.2 s, are acquired in succession. Colourscale plots are obtained by compiling these spectra such that λ in nm is plotted on the y-axis against time in seconds on

33

the x-axis. Intensity in the transmission spectra is manifest as the literal brightness intensity of each track against the background.
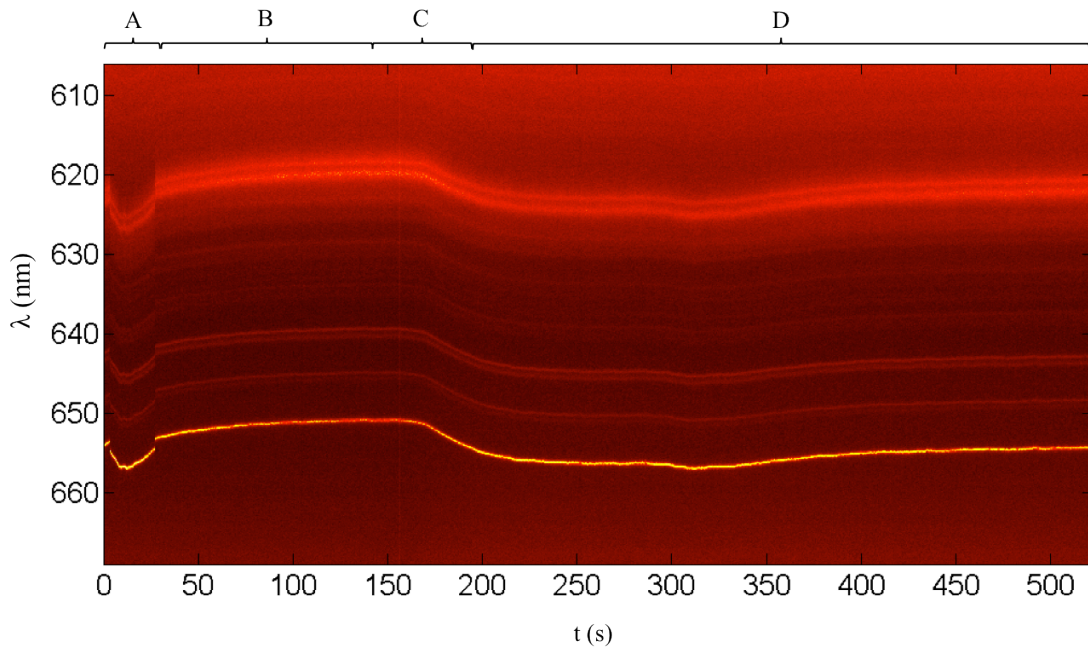

Figure 16: *Colourscale plot for L = 2.267 microns*

The brightest line at the bottom represents the longitudinal modes, where the fainter lines above are the transverse modes. The lower intensity of the transverse modes is because transverse excitation is emitted at an angle to the objective lens, which in turn has an angle cut off so transverse modes appear to have a depleted intensity on the colourscale plot. Longitudinal modes emit along the same axis as the objective without any angle, and therefore appear the brightest. In the theoretical discussion, transverse mode components were ignored in calculations, so we focus only on the longitudinal track. In order to explain the shape of the line, the plot has been divided up into regions. Region A marks the beginning of the experiment where the syringe is being plugged in and saline solution is being injected. The discontinuity and sharp curve are as a result of the tubes being handled. In region B the wavelength starts to flatten out as the cavity length relaxes and settles. Region C records the point at which saline has reached the cavities and the resonant wavelength shift. In Region D the cavity has been completely flooded with salt solution, and the system is restabilising within the new saline environment.
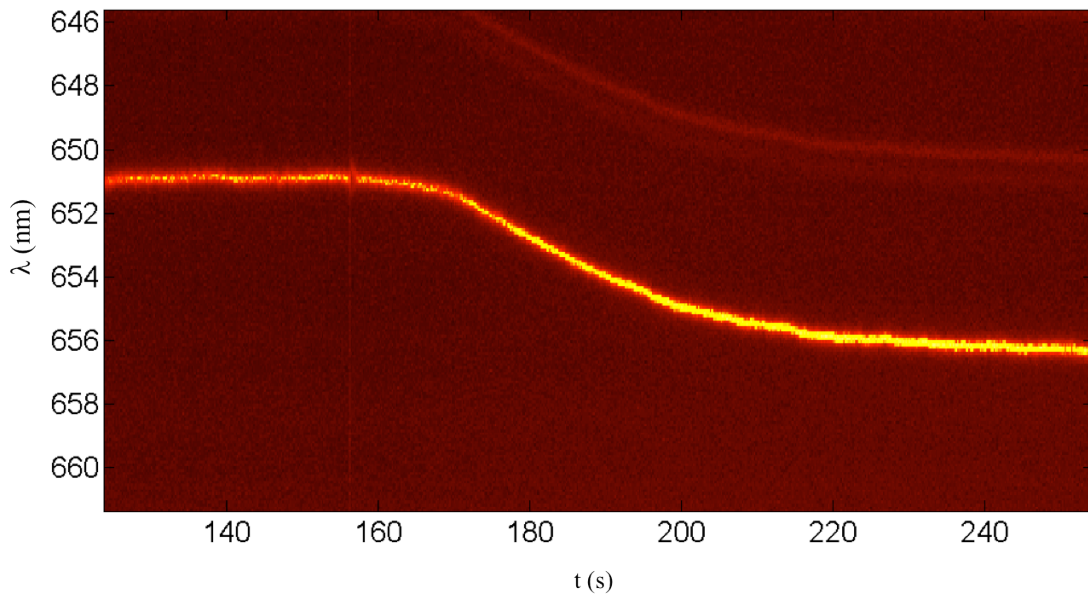
Figure 17: *Focus on the region of the resonant shift*

By zooming in on the region of the shift, it is possible to measure a change in wavelength of approximately 5 nm. By superimposing all the resonant shifts onto a single graph, the time delay becomes evident in the lateral distribution of the tracks.
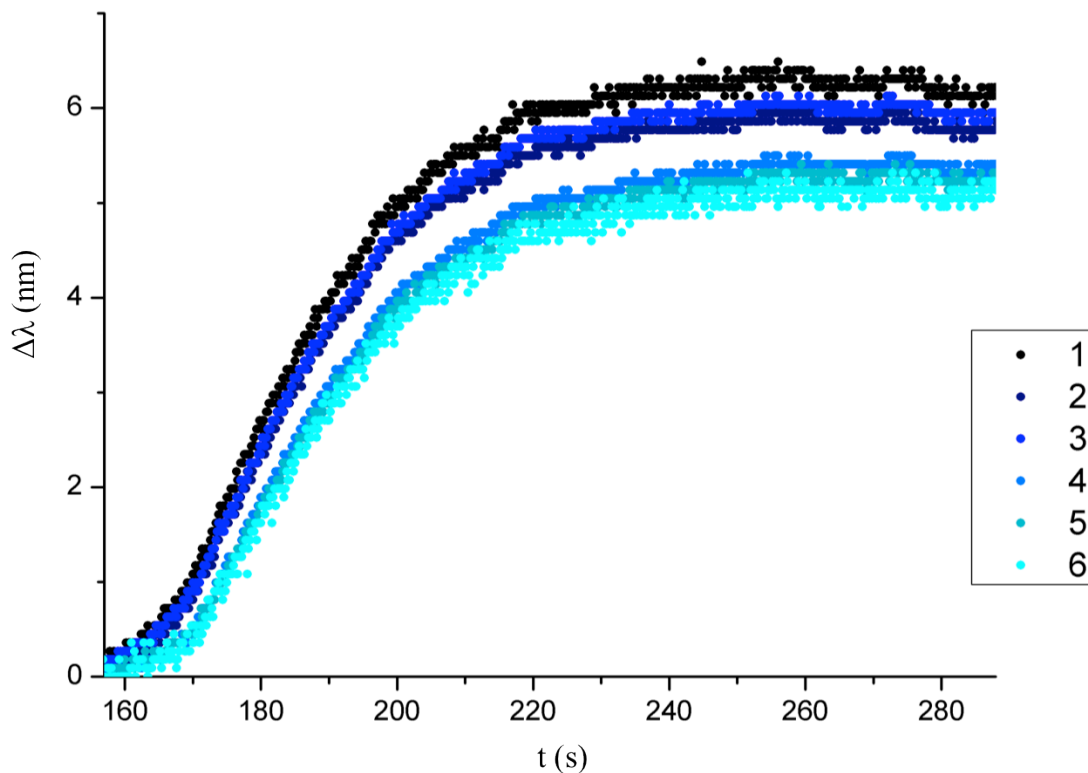

Figure 18: *Graph showing time delay of salt arriving in the cavity across a series of lengths*

Unexpectedly, despite tracking modes from cavities with very similar cavity lengths, the shift recorded is slightly different. A spread from the time delay is still evident. This is quantified

by taking the time at $\dfrac{\Delta\lambda}{2}$ for each track. A time delay of 5 seconds is observed. This shift is in the order of the saline solution flow. It was initially thought this equates to the flow of the syringe pump at 0.2 L/min, but a calculation of the diffusion coefficient of the salt indicates that it could be a function of this as well. Either way it appears that this is as a result of the salt entering the cavities.

Table 3: *Time at which half the total mode shift occurs*

Track	$\dfrac{\Delta\lambda}{2}$	t (s)
1	3.1545	183.2
2	2.925	184.8
3	3.0195	184.4
4	2.704	186.4
5	2.636	187
6	2.567	188.2

4.3   Length Dependent Resonant Shift Investigations

To further characterize the new device, a series of length dependent experiments were carried out. As in the first experiment, the cavities were aligned along the slit of the CCD. This time a high tilt angle between the planar and hemispherical mirrors was introduced along the propagation axis of the saline solution, such that a series of lengths could be imaged at the same time.

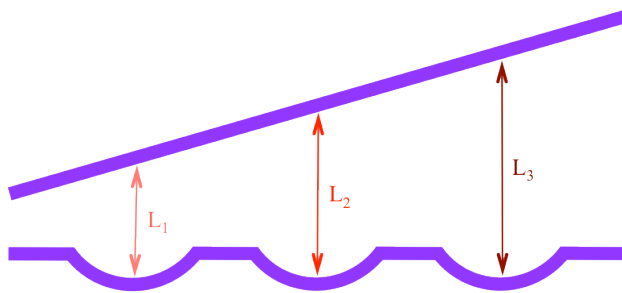**Figure 19:** *Mirror configuration with high tilt to obtain a series of different cavity lengths*

The syringe pump was set to inject at a rate of 0.2 mL/min. The experiment was repeated three times with three different saline concentrations; 13, 15 and 20 g/100 mL. As postulated in the theoretical discussion, a compensation factor was expected.

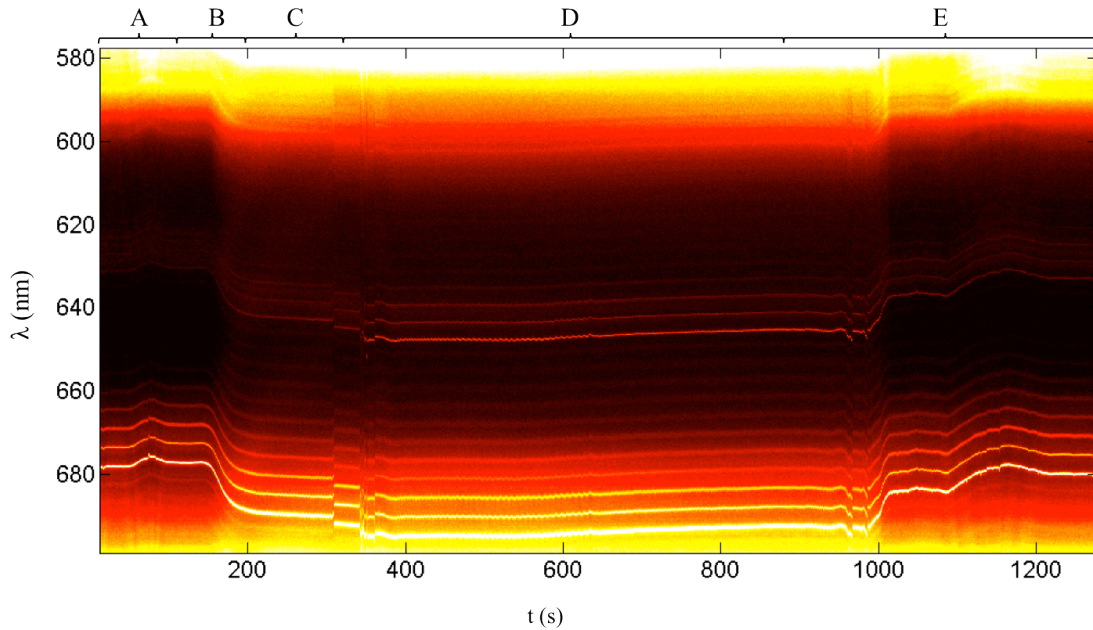As in the length independent experiment, colourscale plots were obtained.

Figure 20: *Colourscale plot from the 20 g/100 mL experiment*

As in figure 16, the bright track at the bottom corresponds to the longitudinal modes, with the subsequently decreasing tracks representing the transverse modes. Region A is where the experiment was being set up and time was being allowed for the cavities to relax. It is clear that although there is a kink in the track in region A, the tracks are much more linear and stable than compared to figure 16. The shift in region B is also quite clean with a clear region of stability in C after the cavities had been flooded with saline solution. In figure 16 a gentle curve is visible, even in the regions where the modes should be stable. This is likely as a result of the setup. In the length dependent set up as shown in figure 17, due to the high tilt, the edge of the mirror substrates were actually in contact at the closed end of the wedge. The pressure from the touching edges results in a much higher degree of cavity length stability. The first set up, however, required the mirrors to be highly parallel and as such were completely open. This makes the system much more liable to cavity instability, especially if the system experienced any pressure changes from the liquid being pumped through. This is something of an intrinsic limitation in the current set up, as truly stable cavity modes can only be achieved if liquid is being forced through the mirrors when the substrates are touching, which necessarily means there must be some angle of tilt between the mirrors. This may be problematic in experiments where parallel mirrors are desired. The noise and discontinuities

at the beginning of region D indicate where the saline syringe has been unplugged and a new syringe of clean water has been coupled in. It was originally intended to confirm the shift was indeed that of saline by attempting to force a shift back to a lower resonant frequency by injecting distilled water back into the system. Analysis of this back shift was abandoned, as the shift was often sporadic and noisy, particularly for higher concentrations of saline, making it difficult to draw meaningful conclusions. This figure is one of the cleanest tracks obtained to demonstrate a back shift. By 1200 s after injecting water back into the cavity, the mode has returned to approximately where it started when the cavity was filled with water around 680 nm. It is also interesting to note in the first half of region D, there appears to be some oscillatory noise. It was found during experimentation that the set up was very sensitive to vibration along the tubing. This noise is likely to be due to the waste tube sitting above the level of liquid in the beaker. Each time a drop formed at the outlet of the tube and dropped into the beaker, the vibrations along the waste tube would be manifest in the results as noise. This could be solved by immersing the end of the tube into the waste liquid such that drops didn't fall off the end. Another likely cause could be from screwing the syringe too tightly into the pump. If it was clamped too tightly, subtle vibrations were propagated down the inlet tubing as the syringe tried to force the plunger through a distorted syringe tube.

From the colourscales, $\Delta\lambda$ values were obtained. As expected from the theoretical discussion in chapter 2, a scaling factor was observed in the data. To reiterate from equation 2.17, the compensation factor f_c is defined as:

$$f_c = \frac{L_{opt} - 2\bar{n}_2 L_{eff}}{L_{opt}}$$

A master plot of f_c against L_{opt} is included below. The blue scatter points represent the raw experimentally obtained data for f_c. The red line represents theoretically calculated values for f_c with L_{eff} calculated from the expression in 2.9. A highly promising fit between the experimental values and the theoretical curve is visible. Particularly promising is the fact that the same theoretical f_c curve with a constant L_{eff} value is superimposed onto experimental data sets across a range of refractive index experiments providing an equally good fit.
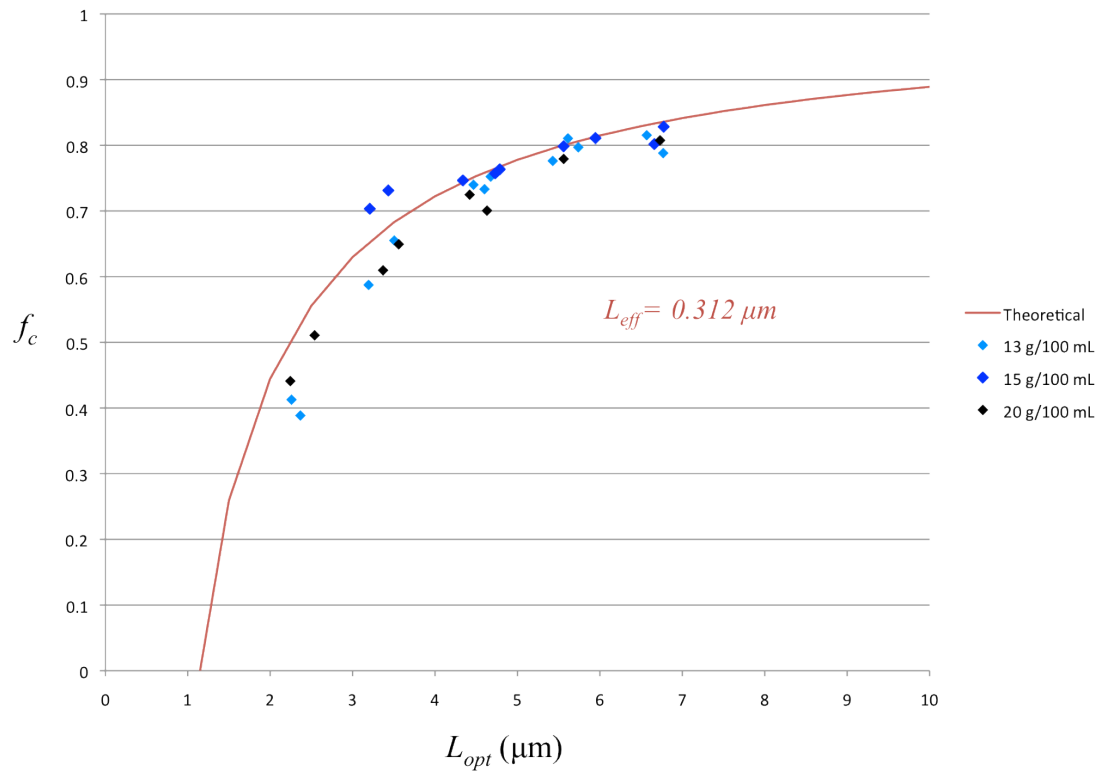
Figure 21: *Graph showing agreement between a theoretical curve for compensation value and experimentally obtained data over a series of different refractive indices*

4.5   Preliminary Device Specifications

A measure of the device's sensitivity S, which can be defined as the wavelength shift per refractive index unit, or $\dfrac{\Delta\lambda}{\Delta n}$, can be obtained. The optimal value of S will obtained for the smallest Δn and the largest corresponding $\Delta\lambda$. The smallest Δn recorded was the shift from water to 13 g/100 mL saline solution which gave Δn=0.0171. The largest $\Delta\lambda$ recorded for this solution was 9.1 μm. This gives a sensitivity of S = 532.03 nm/RIU. Compared to some of the sensitivity values quoted in section 1, this is device is almost 5 times more sensitive [8].

For a better idea of the amount of impurity being detected in this set up we can calculate the number of molecules present. The mode volume of a cavity is approximately 1 μm^3 [1]. In

this volume, the device is able to sense the presence of 1.3×10^9 molecules of NaCl. This is

the equivalent of 1.296×10^{-13} g of salt.

5   Conclusion

In this report, the results of refractive index sensing of open access microcavities have been presented. In section 2, a theoretical model to predict a resonant shift as a function of refractive index was developed. Included in the model was an accurate consideration of the effect of the penetration depth of the DBR on the measured shift. This model was supported by the results obtained in section 4. A penetration depth of 0.312 nm was calculated from the theoretical model. The results displayed demonstrate the first successful results to sense an impurity in liquid using these particular open access microcavities. Successful resonance shifts were observed for saline solution of 13, 15 and 20 g/ 100mL saline solutions. A novel flow cell design used to obtain the results in section 4 was presented in section 3. In this conclusion some weaknesses of the current set up are discussed including systemic noise. The section ends with an outlook towards the future of this device.

5.1   Design Weaknesses

The following section, highlights some of the weaknesses of the setup, as well as some alternatives that might be taken into consideration if a further iteration of this design were to be produced.

As the purpose of the flow cell was to create an aqueous environment for the cavities to surround, the design could be deemed a success if minimal leaking was observed and fluid was flowing through the cavities. While leaking was stemmed by using extra materials such as thread tape, most of the leaking initially observed could be rectified by modifications to the original design, if a second stage prototype were to be made.

Owing to the diminutive thickness of the bottom plate and the stress concentration towards the centre of the cell from the actuator, flexing was observed at the ends of the plate. This opened up gaps for leaking. Bulldog clips were used as a 'band-aid solution' to prevent the bottom plate from winging, and provide a uniform compression across the whole cell. Briefly perusing the dimensions of the top plate in figure 6, it is clear that the region available to be clipped was a matter of millimeters, which proved to be dangerous as the spring loaded

bulldog clips could easily fly off the setup. A modification to the original design might include increasing the surface area at the ends of the plate and including custom clamps.

The silicone rubber purchased was also quite stiff and required quite a high degree of compressive force to ensure the seal performed as intended. This proved problematic at times as the components had to be braced incredibly tightly against the cage rods to prevent sliding of the actuator during compression. A lower stiffness alternative such as PDMS might be more appropriate in a second iteration of this design.

The silver dag adhesive was cumbersome as, after being submerged in water for extended periods of time, it debonded from the coverslip every time the cell was disassembled after a day of experimentation. Although the cleaning and remounting process was time consuming, a non-permanent bond was still used for the duration of this project as there is the risk that low viscosity adhesives might seep underneath the cavities, which would interfere with the light path. In a second iteration a permanent adhesive is recommended.

These comments apply mainly to immediate upgrades that could be made to the device. A long term view on upgrades is discussed in 5.3.

5.2   Systemic Noise

As mentioned previously, this set up is very sensitive to ambient vibrational noise. When the cavities are stable, noise is not a huge issue. We can estimate the noise by looking at the linewidth of the colourscales. The minimum linewidth is 0.1 nm. In the case of the colourscales it appears that noise analysis is resolution limited as the linewidth appears to have the width of a pixel when zooming into a colourscale. This implies that as long as the cavities are touching, extremely stable modes can be obtained.

Noise is of course introduced if components of the system are subject to movement. The major source of vibrational movement came from tubes as they were directly connected to the mirror mount and were most liable to be touched as they were dangling in free space.

The method of coupling fluid in and out of the system was particularly rudimentary. A more rigorous interpretation of the tubing system would be necessary in further experimentation.

For the duration of this project, when spectral videos were being acquired and a different fluid was to be injected into the cavity, the tubes were decoupled by hand from one syringe to another, which led to a lot of unanalysable noise being introduced into the system. In these experiments the problem was mitigated by allowing substantial time for the cavities to restabilise before pumping the new syringe. Purchasing microfluidic connections such as T-junctions would enable multiple syringes to be connected into the line. While the automated infusion pump was only being used to pump one syringe at a time, the model used had a programmable interface which could be used in the future to co-ordinate the pumping of different syringes loaded with fluids of different refractive index.

5.3   Future Directions

In the immediate future, there a number of modifications that could be made to the current design for further testing. The device could be used for different types of sensing testing. This project focused on a resonant shift. Other experiments that could be carried out with the device include testing the absorption capabilities by injecting a lasing dye into the cavity and later observing colour reactions from dissolved gases in water or testing fluorescence enhancement as a result of the Purcell effect [8].

This device would benefit from a more sophisticated microfluidic system. Integration into lab-on-a-chip device would be the natural evolution [19].

Project Management

It became clear from the outset of this project that I was going to need to rely heavily on the expertise of others as this project demanded a knowledge base and skill set that I had not gained from my first three years of study in my undergraduate course. I learned that time management was an extremely crucial skill to have when liaising with so many parties, as well as being able to make executive decisions to prevent my project from digressing from the main aim.

As part of a relatively small group with a diverse range of projects, no single person had a completely exhaustive understanding of all aspects of my project. When seeking help, I sought to identify colleagues whose work paralleled the question I was aiming to ask. I found that although asking questions was extremely important, attentive listening was paramount in respecting everyone's demanding schedules.

The first part of Michaelmas was spent being trained to use the focused ion beam (FIB) microscope so that I could reproduce the cavities produced by former group member Phil Dolan, as outlined in his thesis. It was originally intended for me to be able to customize and mill my own cavities for use in the device I was creating. I was also enrolled into a short course in scanning electron microscopy (SEM), as the principles of operation were similar to the imaging system used in FIB. Atomic force microscopy (AFM) training also followed on from this as it was found that some method of characterizing the milled cavities was necessary. As both FIB and AFM are shared resources throughout the department, forward planning and time management were important, as during term time both instruments could be fully booked up to two weeks in advance. Throughout the term, it became evident that reproducing the cavities was more complicated than originally envisioned, and FIB milling became a research topic in its own right. Although I had the option to further pursue the milling process, ultimately the crux of my project hinged around exploring the sensing capabilities of cavities rather than trying to perfect their morphology. As a result, despite

quite extensive training on FIB and AFM, a decision was made to hand over this aspect of the project to another more permanent group member.

Effective time management became particularly important when juggling purchase orders and sending manufacturing jobs to the workshop in order to produce my final design. After finalizing the design of the flow cell on paper, it took another three weeks before a physical manifestation existed in the lab. I was limited by the fact that in the department workshop there was only one technician with the skills required for such a small scale device, who was only available one day a week. I ensured I arranged preliminary meetings with him before presenting with him with the final design to ensure the workshop was stocked with the appropriate materials, and that his schedule would allow time to complete the manufacture of my design. In these meetings I was made aware of the limitations of some of the machines used in the workshop and I consequently had to alter the thread positioning in one component of my device as it was impossible to machine a thread at the dimensions I had requested.

At the same time as I was waiting for the workshop to machine my components, I was sending purchase orders for my fluidic components and silicone rubber. Although it would have been difficult to speed up the work rate of the workshop considering the number of hours the technician I required was working, in retrospect I could have placed my purchase orders earlier, especially the order for the fluidic components as they had to be ordered from America.

Time management was still important after the device had been fabricated in the workshop, as the spectrometer and white light source necessary for my project was a shared resource within the group. Each week, there were four people, including myself, who needed to make use of the set up. A timetable with allocated lab sessions was utilised, and I learned the importance of being on time to maximize my time on the set up. At the beginning of my time in the lab, I was still booking FIB sessions, which often clashed with my allocated lab sessions. To achieve an even balance between lab time and FIB sessions, clear communication with my other colleagues was important so we could swap lab sessions at mutually agreeable times.

Clear communication was also important as this project was a collaboration with Dr Claire Vallance's group in the chemistry department. Termly meetings were held to compare ideas. These meetings were helpful in problem solving as questions commonly approached by members of this group from a physics standpoint were attacked from a chemist's standpoint. The collaboration was also extremely helpful for borrowing apparatus; where a syringe pump was more difficult to find in nearby materials labs, the injection system was an extremely common tool in a wet chemistry lab.

Bibliography

[1]   Dolan. P 2012 Ultra-Small Open Access Microcavities for Enhancement of the Light-Matter Interaction. PhD thesis, University of Oxford

[2]   P. Jiang, X. H. (2006) Fabrication of Two-Dimensional Organic Photonic Crystal Microcavity. Chinese Physics Letters, 23, 7, 1813-1815

[3]   M. Kahl, T. T (2007) Colloidal Quantum Dots in All-Dielectric High-Q Pillar Microcavities. Nano Letters 7, 9, 2897-2900

[4]   F. Ay, J. D. B. B, (2009) Optical performance investigation of focused ion beam nanostructured integrated Fabry-Perot microcavities in Al_2O_3 In: European Conference on Lasers and Electro-Optics 2009 and the European Quantum Electronics Conference, CLEO Europe - EQEC 2009, 14-19 June 2009, Munich, Germany.

[5]   F. Vollmer, D. B. (2002). Protein detection by optical shift of a resonant microcavity. Applied Physics Letters, 80, 4057

[6]   M. A. Vincenti, M. D. (2007). Fabry-Pérot microcavity sensor for H2-breath-test analysis. Journal of Applied Physics, 102, 074501.

[7]   Y. Guo, K. R. (2011). Optofluidic Fabry-Pérot cavity biosensor with integrated flow-through micro-/nanochannels. Applied Physics Letters, 98, 041104.

[8]   D. Dorfner, T. Z. (2009). Photonic crystal nanostructures for optical biosensing applications. Biosensors and Bioelectronics, 24, 3688-3692.

[9]   S. Tomljenovic- Hanic, C. MdS. (2013) Reconfigurable, Defect-Free, Ultrahigh-Q Photonic Crystal Microcavities for Sensing. Sensors 2013, 13, 3262-3269

[10]   Amarie D, Glazier JA. Label-Free Microcavity Biosensors: Steps towards Personalized Medicine. *Sensors*. 2012; 12(12):17262-17294.

[11]   T. Yoshie, L. T. (2011) Optical Microcavity: Sensing down to Single Molecules and Atoms. Sensors, 11, 1972-1991

[12]   K. Vahala (2003). Optical microcavities. Nature 424, 839-846

[13]   F. Vollmer, L. Y. (2012). Label-free detection with high-Q microcavities: a review of biosensing mechanisms for integrated devices. Nanophotonics 1, 267-291

[14]   L.R.Brovelli, U. K. (1995). Simple analytical expressions for the reflectivity and the penetration depth of a Bragg mirror between arbitrary media. Optics Communications 116 (1995) 343-350

[15]   P. Dolan, G. H. (2010) Femtoliter tunable optical cavity arrays. Optics Letters, 35(21):3556-8

[16]   http://www.qualcommtricorderxprize.org/competition-details/overview

[17]   http://www.topac.com/salinity_brix.html

[18]   M. O'Toole , D. D. (2008) Sensors, 8, 2453

[19]   Y. Cao, Y. Z. (2012) Efficient Optical Pattern Detection for Microcavity Sensors Based Lab-on-a-chip. Sensors, 12, 6, 2121-2128